# Binding, Unbinding and Aggregation of Crescent-Shaped Nanoparticles on Nanoscale Tubular Membranes*

Eric J. Spangler, Alexander D. Olinger
*Department of Biomedical Engineering and Department of Physics and Materials Science, The University of Memphis, Memphis, TN 38152, USA*

P.B. Sunil Kumar
*Department of Physics, Indian Institute of Technology Palakkad, Palakkad-668557, Kerala, India*

Mohamed Laradji †
*Department of Physics and Materials Science, The University of Memphis, Memphis, TN 38152, USA*

Using molecular dynamics simulations of a coarse-grained implicit solvent model, we investigate the binding of crescent-shaped nanoparticles (NPs) on tubular lipid membranes. The NPs adhere to the membrane through their concave side. We found that the binding/unbinding transition is first-order, with the threshold binding energy being higher that the unbinding threshold, and the energy barrier between the bound and unbound states at the transition that increases with increasing the NP's arclength $L_{np}$ or curvature mismatch $\mu = R_c/R_{np}$, where $R_c$ and $R_{np}$ are the radii of curvature of the tubular membrane and the NP, respectively. Furthermore, we found that the threshold binding energy increases with increasing either $L_{np}$ or c$\mu$. NPs with curvature larger than that of the tubule ($\mu > 1$) lie perpendicularly to the tubule's axis. However, for $\mu$ smaller than a specific arclength-dependent mismatch $\mu^*$, the NPs are tilted with respect to the tubule's axis, with the tilt angle that increases with decreasing $\mu$. We also investigated the self-assembly of the NPs on the tubule at relatively weak adhesion strength and found that for $\mu > 1$ and high values of $L_{np}$, the NPs self-assemble into linear chains, and lie side-by-side. For $\mu < \mu^*$, and high $L_{np}$, the NPs also self-assemble into chains, while being tilted with respect to the tubule's axis.

## I. INTRODUCTION

The understanding of the effect of nanoparticles (NPs) geometry and surface properties on their interaction with biomembranes is important to the development of effective and safe nanomaterials for biomedical applications such as biosensing [1], gene therapy [2], diagnostics [3], targeted drug delivery [4], photothermal therapy [5] and magnetic hyperthemal therapy [6]. This understanding is also important to the mitigation of health and environmental hazards of some nanomaterials [7]. The adhesion of nanoscale biomolecules or synthetic NPs on biomembranes, resulting from attractive forces between these and the lipid head groups or specific receptors on the membrane, often leads to morphological deformations of the membrane, which depend strongly on the size, geometry and surface properties of the adhered particles as well as the elasticity of the membrane [8, 9, 11–14].

Many studies have been performed in the past to investigate the adhesion of convex NPs, schematically shown by Fig. 1 (A, B), with different geometries, such as nanospheres [11, 12, 15–24], nanoellipsoids [25, 26], nanocylinders [9], nanospherocylinders [9, 10], nanocubes [9], as well as Janus NPs [27, 28] on biomembranes. A general feature of these NPs is that, due to their convex shape, they can easily adhere to the membrane, regardless of the difference between the curvature of the NP and that of the membrane [21, 24]. The binding process of such NPs begins with the adhesion of a small surface of the NP on the membrane followed by a complete or partial wrapping of the NP by the membrane to a degree determined by the interplay between the adhesion strength, the geometry and size of the NP, and elasticity of the membrane [11, 12, 15, 16, 21, 24]. Although NPs generically similar to those in Fig. 1 (A) can be fully wrapped and en-

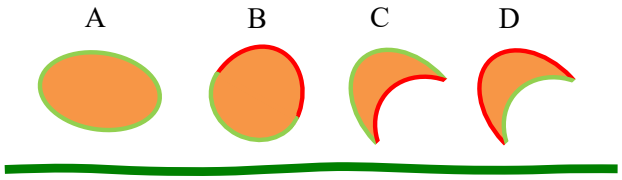


FIG. 1: Four general NP structures interacting with a lipid bilayer (dark green). The light green (red) region of the NP interacts attractively (repulsively) with the membrane. (A) corresponds to a convex NP with a uniform surface that interacts attractively with the membrane. (B) corresponds to a convex Janus NP with one moiety that interacts attractively with the membrane and the other moiety interacts repulsively with the membrane. (C) corresponds to a Janus concavo-convex NP which interacts attractively with the membrane through its convex side only. (D) corresponds to a Janus concavo-convex NP which interacts attractively with the membrane through its concave side only.

*Submitted to Soft Matter January 19, 2021
†Email: mlaradji@memphis.edu

docytosed by the membrane [21, 24, 26], Janus NPs similar to those in Fig. 1 (B) can only be partially wrapped by the membrane [27, 28]. An interesting situation emerges in the case of Janus concavo-convex (JCC) NPs, such as those shown schematically in Fig. 1 (C, D). A JCC NP that interacts attractively with the membrane through its convex side (e.g. Fig. 1 (C)) will easily adheres to the membrane in a manner similar to convex NPs, schematically shown by Fig. 1 (A, B) [27]. However, the adhesion process of a JCC NP to a membrane through its concave side (Fig. 1 (D)) is not clear. In particular, it is not clear whether the binding of JCC NPs on lipid membranes is discontinuous and the effect that the NP's arclength and curvature have on the binding transition.

An example of nanoscale particles, which interact attractively with lipid membranes through their concave side, corresponds to a family of membrane proteins known as Bin-Amphyphisin-Rvs (BAR) domain proteins [29]. BAR domain proteins have a complex structure which includes a bundle of positively charged alpha-helical coils that are arranged in a crescent-shaped dimer, giving them an anisotropically curved shape. This allows them to adhere to negatively charged lipid membranes and generate curvature [30]. The curvature of BAR domains may be high, such as the case of the N-BAR domain proteins [31], gentle, such as the case of the F-BAR domain proteins [32], or even negative, such as the case of the I-BAR domain proteins [33]. BAR domain proteins are ubiquitously found in many parts of eukaryotic cells, and are important to many cellular processes, including cell motility, endocytosis, cytokinesis, intracellular trafficking, and in the shaping of cellular organelles such as the endoplasmic reticulum and the Golgi body [30, 34].

Much of the microscopic details of the interaction between BAR domain proteins and lipid membranes have been obtained through atomistic molecular dynamics simulations [35–38] and coarse-grained molecular dynamics simulations [36–43]. Atomic-scale simulations provide a detailed picture of the interaction between an individual BAR domain and a specific lipid bilayer, including the time scale it takes for the protein to fully bind to the membrane [38] and the effects of the protein's binding on the local lipid density [36] and local membrane curvature [36, 38]. However, the high computational cost of atomistic molecular dynamics simulations of BAR domain proteins does not allow for investigating their cooperative behavior on the long-wavelength morphology of lipid membranes. These can be inferred from coarse-grained molecular dynamics simulations of self-assembled lipid membranes [36–43]. These simulations have shown that the adhesion of the BAR domain proteins leads to their self-assembly, despite the repulsive protein-protein interactions, and results in dramatic morphological changes of the membrane. There are many outstanding question in regard to the effect of BAR domain proteins interaction with lipid membrane, particularly in regard to what aspects of the domains are responsible for curvature sensing and generation [34].

BAR domains are complex and interact with lipid membranes through a heterogeneous interface. In addition, BAR domains usually interact with lipid membranes through amphipathic residues that insert in the hydrophobic core of the membrane. BAR-domain proteins might not therefore be ideally suitable for the understanding of the interaction of anisotropically curved nanoscale particles, such as JCC NPs, with lipid membranes. Such understanding has been attempted through coarse-grained Monte Carlo simulations of dynamically triangulated membranes, where the curvature-generating NPs are treated as isotropic [44] or anisotropic fields [46, 47] with short-range attractive interactions. While allowing for the investigation of the long-wavelength effect of these fields on the morphology of lipid membranes, this approach cannot infer the effect of anisotropically curved NPs on the membrane at the microscopic level. Furthermore, the results from this approach depend strongly on the details of the model [48]. In another less coarse-grained approach, the anisotropically curved NPs are treated as intrinsically part of the membrane with a preferred anisotropic curvature [49, 50]. A disadvantage of this model is that the proteins cannot bind or unbind to the membrane, and their adhesion strength is ill-defined. More recently, our group introduced a relatively simple coarse-grained approach based on self-assembled lipid membranes [51], in which the curvature-generating agents are treated as explicit anisotropically curved crescent-shaped NPs, shown in Fig. 2, that interact attractively with the lipids head groups through their concave side [52]. For simplicity, the concave surface of these NPs is treated as homogeneous without amphipathic complexes that insert in the hydrophobic side of the membrane, as is the case of the N-BAR domain proteins. The goal of this study was not to specifically investigate BAR domain proteins interaction with lipid membranes. Instead, our goal was to investigate the interaction of generic anisotropically curved NPs with lipid membranes. Molecular dynamics simulations of this model in the case of closed vesicles showed that, for weak adhesion strength, the NPs aggregate into linear chains, in which the NPs self-assemble side-by-side [52]. At high adhesion strength, the NPs induce local saddle regions, leading to their self-assembly into star-like networks on the vesicle [52].

In the present article, we extend our earlier study in [52] to investigate the binding and unbinding of crescent-shaped NPs, and their aggregation on tubular membranes. In Section III A, we show that the binding-unbinding transition is first-order, with the binding of the NPs requiring a higher adhesion energy per unit area than their unbinding. Furthermore, both binding and unbinding adhesion energy thresholds increase with increasing the curvature mismatch, $\mu = R_c/R_{np}$, where $R_c$ and $R_{np}$ are the radii of curvature of the tubular membrane and NPs, respectively, or increasing the NPs arclength, $L_{np}$. In Section III B, the mode of bind-

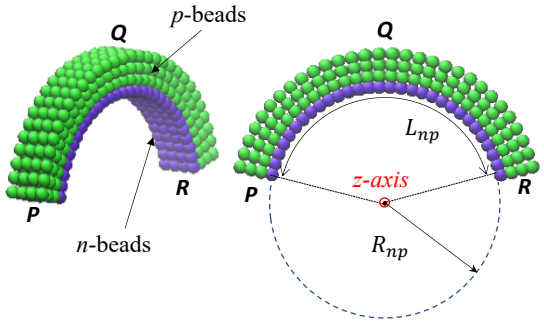


FIG. 2: Two views of a crescent-shaped NP of radius $R_{np}$ and arclength $L_{np}$. The $n$-beads (purple beads) on the concave surface of the NP interact attractively with the lipid head beads but repulsively with the lipid tail beads, promoting adhesion of the NP on the lipid membrane. The $p$-beads (green beads) interact repulsively with all lipid beads. The points $P$ and $R$ indicate locations on the ends of the NP, and the point $Q$ is at the apex of the NP.

ing of crescent-shaped NPs on tubular membranes is investigated as a function of $\mu$ and $L_{np}$. We show that for $\mu > 1$, NPs lie perpendicularly to the tubule's axis. However, for $\mu$ smaller than a certain $L_{np}$-dependent curvature mismatch $\mu^* < 1$, NPs are tilted with respect to the tubule's axis, with an average tilt angle that increases with decreasing $\mu$ or increasing $L_{np}$. Finally, in Section III C, we investigate the spatial arrangement of many NPs on tubular membranes and found that they form linear chains, with the NPs aligned side-by-side, for $\mu \gtrsim 1$, or $\mu < \mu^*$, and high $L_{np}$. However for low values of $L_{np}$ or for $\mu^* < \mu \lesssim 1$, the NPs are distributed more uniformly on the tubule.

## II. MODEL AND APPROACH

Here, we use a coarse-grained implicit-solvent model that allows for the self-assembly of lipid membranes. The details of this model was presented earlier in Refs. [51, 53]. The same model was used in our previous study of membrane-induced aggregation of crescent-shaped NPs [52]. Briefly, a lipid molecule is coarse-grained in this model into a chain of one hydrophilic (head) bead and two hydrophobic (tail) beads. The anisotropically curved crescent-shaped NPs are modeled as a composite of two types of beads, as shown in Fig. 2. The interaction potential energy of the composite membrane-NPs system is given by

$$U(\{\mathbf{r}_i\}) = \sum_{i,j} U^0_{\alpha_i\alpha_j}(r_{ij}) + \sum_i \sum_{j\in\Omega_i} U^{\rm bond}_{\alpha_i\alpha_j}(r_{ij}) + \sum_i \sum_{j\in\Omega_i} \sum_{k\in\Omega_i} U^{\rm bend}_{\alpha_i\alpha_j\alpha_k}(\mathbf{r}_i,\mathbf{r}_j,\mathbf{r}_k), \quad (1)$$

where $\mathbf{r}_i$ is the position of bead $i$ and $r_{ij} = |\mathbf{r}_j - \mathbf{r}_i|$. The type of bead $i$, $\alpha_i = h$, $t$, $n$ or $p$ for lipid head beads, lipid tail beads, NP bottom layer beads (purple beads in Fig. 2), or other NP beads (green beads in Fig. 2), respectively. $\Omega_i$ is the set of beads bonded to $i$. In Eq. (1), $U^0_{ij}$ is modeled by a soft two-body interaction, between beads $i$ and $j$, that depends on the types of the two beads, $\alpha_i$ and $\alpha_j$, and is given by the piecewise function,

$$U^0_{\alpha_i\alpha_j}(r_{ij}) = \begin{cases} (U^{\rm max}_{\alpha_i\alpha_j} - U^{\rm min}_{\alpha_i\alpha_j})\frac{(r_m - r_{ij})^2}{r_m^2} + U^{\rm min}_{\alpha_i\alpha_j} & \text{if} \quad r_{ij} \le r_m, \\ -2U^{\rm min}_{\alpha_i\alpha_j}\frac{(r_c - r_{ij})^3}{(r_c - r_m)^3} + 3U^{\rm min}_{\alpha_i\alpha_j}\frac{(r_c - r_{ij})^2}{(r_c - r_m)^2} & \text{if} \quad r_m < r_{ij} \le r_c, \\ 0 & \text{if} \quad r_{ij} > r_c, \end{cases} \quad (2)$$

where $U^{\rm max}_{\alpha\beta} > 0$ for any pair $(\alpha, \beta)$ and $U^{\rm min}_{hh} = U^{\rm min}_{ht} = 0$. Since the solvent is implicit in this model, the self-assembly of the lipids into stable bilayers can be achieved by setting $U^{\rm min}_{tt} < 0$ [51].

In addition to the interaction given in Eq. (2), beads that belong to a single lipid molecule or a NP are linked through $U^{\rm bond}_{\alpha_i\alpha_j}$ given by

$$U^{\rm bond}_{\alpha_i\alpha_j}(r_{ij}) = \frac{k^{\rm bond}_{\alpha_i\alpha_j}}{2}(r_{ij} - a_{ij})^2, \quad (3)$$

where $k^{\rm bond}_{\alpha_i\alpha_j}$ is the stiffness of the bond between $i$ and $j$. The bending stiffness of the lipid molecules and the rigidity of the NPs are maintained by the three-body interaction $U^{\rm bend}_{ikl}$ which is given by,

$$U^{\rm bend}_{\alpha_i\alpha_j\alpha_k}(\mathbf{r}_i,\mathbf{r}_j,\mathbf{r}_k) = \frac{k^{\rm bend}_{\alpha_i\alpha_j\alpha_k}}{2}\left(\cos\theta^0_{ijk} - \hat{\mathbf{r}}_{ij}\cdot\hat{\mathbf{r}}_{ik}\right)^2, \quad (4)$$

where $k^{\rm bend}_{\alpha_i\alpha_j\alpha_k}$ and $\theta^0_{ijk}$ are the bending stiffness of a triplet $(i, j, k)$ and its preferred splay angle, respectively, and $\hat{r}_{ij} = (\mathbf{r}_j - \mathbf{r}_i)/|\mathbf{r}_j - \mathbf{r}_i|$. The interaction parameters of the lipids are given by $U^{\rm max}_{hh} = U^{\rm max}_{ht} = 100\epsilon$, $U^{\rm max}_{tt} = 200\epsilon$, $U^{\rm min}_{hh} = U^{\rm min}_{ht} = 0$, $U^{\rm min}_{tt} = -6\epsilon$, $k^{\rm bond} = 100\epsilon/r_m^2$, $k^{\rm bend} = 100\epsilon$, $r_c = 2r_m$, $a = 0.7r_m$ and $\theta_0 = 180^o$. In the present study we limit ourselves to membranes with cylindrical geometry.

A crescent-shaped NP is composed of beads that are arranged in a curved simple cubic lattice, as shown by

Fig. 2. The beads within a NP are linked via the bonding interaction, Eq. (3), with $k^{\rm bond} = 1600\epsilon/r_m^2$. The curvature of a NP is induced by adjusting the preferred bond length, along the tangential (curvilinear) direction, of the $n$th plane of the NP according to

$$a_n^{tan} = a_1 \left[1 + (n-1)\frac{a_1}{R_{np}}\right], \text{ with } n = 1,\ 2,\ \cdots, \quad (5)$$

where $R_{np}$ is the NP's radius of curvature $a_1 = 1.0 r_m$ is the preferred bond length of the concave (purple) plane in Fig. 2. The preferred bond lengths along the axial and radial directions are both kept at $a_1$. The NP beads are also linked via the bending interaction, Eq. (3), with $k^{\rm bend} = 1600\epsilon$. The preferred angle $\theta^0_{ijk} = 90^o$ or $180^o$ if all three beads $i$, $k$ and $l$ are along the same radial direction or along the $z$-axis, as indicated in Fig. 2. Otherwise, $\theta^0_{ijk} = 2\cos^{-1}(a_1/2R_{np})$ or $\theta^0_{ijk} = 180^0 - \cos^{-1}(a_1/2R_{np})$.

Since we are interested in the case of NPs which prefer to adhere to the lipid membrane through their concave side, we set $U^{\rm min}_{hn} = -\xi < 0$ and $U^{\rm min}_{hp} = 0$ to minimize NPs' adhesion through their convex side. Insertion of the NPs in the hydrophobic region of the membrane is prevented by setting $U^{\rm min}_{tn} = U^{\rm min}_{tp} = 0$. $U^{\rm max} > 0$ for all $nh$, $nt$, $ph$ and $pt$ pairs. Henceforth, $\xi$ is used as a measure of the strength of the adhesive interaction between the NP and the membrane. For pairs of beads belonging to the same NP, we set $U^{\rm min}_{nn} = U^{\rm min}_{pp} = U^{\rm min}_{pp} = 0$ and $U^{\rm max}_{nn} = U^{\rm max}_{pp} = U^{\rm max}_{pp} = 0$. In order to prevent the NPs from aggregating in the absence of lipid membranes, interactions between two beads belonging to different NPs are fully repulsive. For these pairs of beads, we set $U^{\rm min}_{nn} = U^{\rm min}_{pp} = U^{\rm min}_{pp} = 0$ and $U^{\rm max}_{nn} = U^{\rm max}_{pp} = U^{\rm max}_{pp} = 100\epsilon$. We consider NPs with three different values of arclength, corresponding $L_{np} = 10$, 20 and 30 nm, and three values of the radius of curvature, corresponding to $R_{np} = 11$, 15 and 19 nm. NPs of length $L_{np} = 10$ nm are composed of 160 beads (40 $n$-beads and 120 $p$-beads), NPs of length $L_{np} = 20$ nm are composed of 320 beads (80 $n$-beads and 240 $p$-beads), and of length $L_{np} = 30$ nm are composed of 480 beads (120 $n$-beads and 360 $p$-beads).

Particles are moved using a molecular dynamics scheme with a Langevin thermostat [54]:

$$\begin{aligned} \dot{\mathbf{r}}_i(t) &= \mathbf{v}_i(t), \text{ and} \\ m\dot{\mathbf{v}}_i(t) &= -\nabla_i U\left(\{\mathbf{r}_i\}\right) - \Gamma \mathbf{v}_i(t) + \sigma \boldsymbol{\Xi}_i(t), \end{aligned} \quad (6)$$

where $m$ is the mass of a each bead (same for all beads), $\Gamma$ is a bead's friction coefficient, and $\sigma\boldsymbol{\Xi}_i(t)$ is a random force originating from the heat bath. $\boldsymbol{\Xi}_i(t)$ obeys

$$\langle \boldsymbol{\Xi}_i(t) \rangle = 0, \quad (7)$$

$$\langle \Xi_i^{(\mu)}(t)\, \Xi_j^{(\nu)}(t') \rangle = \delta_{\mu\nu}\delta_{ij}\delta(t-t'), \quad (8)$$

with $\mu$, $\nu = x$, $y$, or $z$. The dissipative and random forces are interrelated through the dissipation-fluctuation theorem, which leads to the relationship

$$\Gamma = \sigma^2/2k_{\rm B}T. \quad (9)$$

The simulations are performed in a box with constant size. In particular, the length of the box along the axis of the lipid tube, $L_z$, is fixed in each simulation, and is set to either $L_z = 30$ nm or 60 nm, depending on the simulation. All simulations are performed at $k_{\rm B}T = 3\epsilon$, a temperature at which the bilayer is in the fluid phase [51]. The equations of motion are numerically integrated using the velocity-Verlet algorithm with $\Gamma = \sqrt{6}m/\tau$ where the timescale $\tau = r_m(m/\epsilon)^{1/2}$ with $r_m$ and $\epsilon$ being used as scales for length and energy, respectively. The time step in all simulations corresponds to $\Delta t = 0.01\tau$. From the comparison of the thickness of our model bilayer in the fluid phase, which is around $4r_m$, with the thickness of a typical fluid phospholipid bilayer, $\sim 4$ nm, we estimate $r_m \approx 1$ nm. Hence, in the remainder of this article, all lengths are expressed in nanometers.

## III. RESULTS

Fig. 3 depicts equilibrium configurations of a single NP, with varying arclength $L_{np}$ and radius of curvature $R_{np}$, on tubular membranes with varying mean radius of curvature $R_c$. Here, $R_c$, is defined as the average radius of the bare tubule measured from the head groups of the outer leaflet. Fig. 3 shows that, in most cases, the NP leads to transverse deformations of the membrane by an extent that depends on the curvature mismatch parameter $\mu = R_c/R_{np}$ and the NP's arclength. Fig. 3 also shows that the NP-induced deformations extend throughout the $z$-axis, owing to the relatively short length of the tubes along the $z$-axis.

We first focus on the case where the curvature of the NP is higher than that of the membrane ($\mu > 1$). A comparison between Fig. 3 (A) and (B), both corresponding to NPs with same arclength but different values of $\mu$ (2.29 for (A) and 1.68 for (B)), shows that the deformation of the membrane increases with increasing $\mu$. A comparison between Fig. 3 (B) and (C), which correspond to NPs with same mismatch parameter ($\mu = 1.68$) but different values of the arclength (30 nm for (B) and 20 nm for (C)), show that the deformation of the membrane also increases with increasing NP's arclength. In particular, Fig. 3 (A-C) show that the cross-section of the tubular membrane becomes more oval as $L_{np}$ or $\mu$ is increased. This is quantified by the transverse curvature, $c_\perp$ of the tubular membrane (curvature in the $xy$-plane) which is calculated as a function of the polar angle, $\phi$, measured from the $y$-axis and with the origin of $xy$-plane corresponding to the center of mass of the tubule (see inset of Fig. 4 (A)). Fig. 4 (A) shows that for very weak mismatch ($\mu = 1.09$), the curvature in the case of a bound NP is identical to the case where the NP is unbound, i.e. the binding of the NP does not affect the tubule's confor-

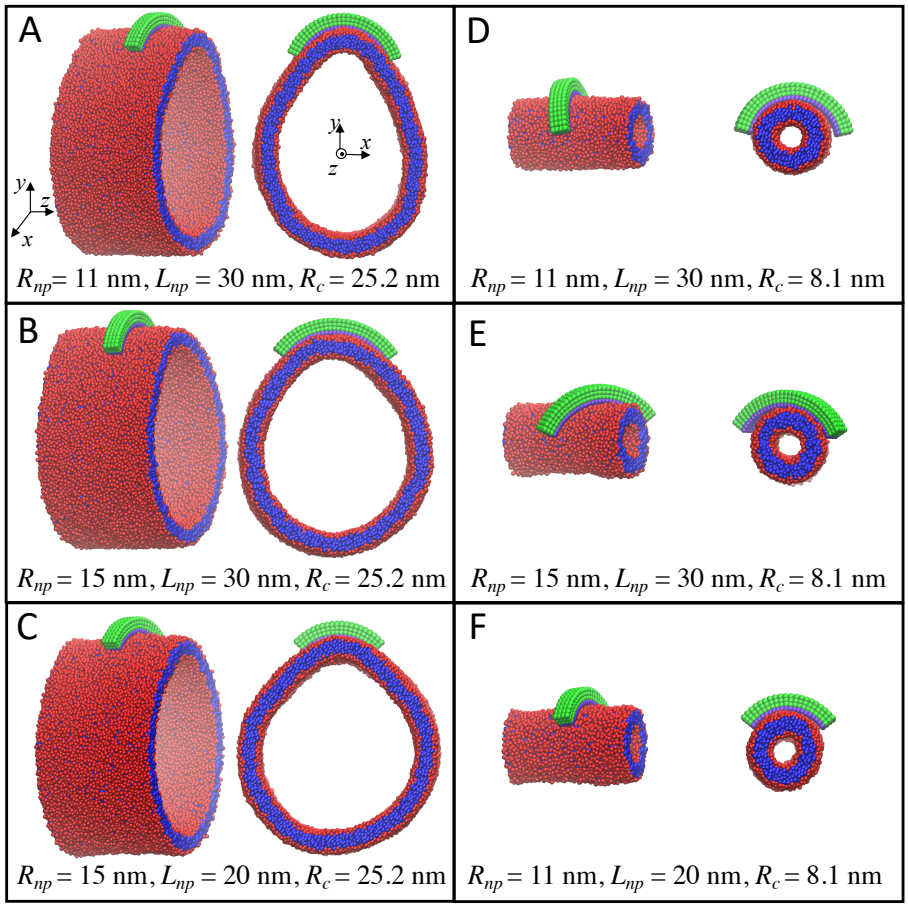


FIG. 3: Side and front equilibrium snapshots of a tubule with a single crescent NP, at different values of $R_{np}$, $L_{np}$ and $R_c$. A, B and C correspond to the case of a tubule with $R_c = 25.2$ nm ($\mu > 1$). D, E and F correspond to the case of $R_c = 8.1$ nm ($\mu < 1$).. The red and blue beads of the tubule correspond to the hydrophilic and hydrophobic beads, respectively.

mation. However for strong mismatch, Figs. 4 (B) and (C), which correspond to $\mu = 1.25$ and 4.36, respectively, show that the adhesion of the NP leads to a significant deformation of the tubule, with the degree of deformation that increases with increasing $\mu$. In particular, both Figs. 4 (B) and (C) show that the curvature of the vesicle follows that of the NP at $\phi \approx 0$. Around the two edges of the NP, $c_\perp$ is smallest, in line with the Figs. 3 (A-C), which show that the tubule tends to be flat around the edges of the NP. As $\phi$ approaches $\pm\pi$, $c_\perp$ then increases, indicating that the bottom of the tubule's cross section is highly curved.

Fig. 3 (D-F) show that the NP's deformation of the membrane is very weak when the radius of the tubular membrane is smaller than that of the NP ($\mu < 1$). While in most cases, the NP's end-to-end vector is perpendicular to the principal axis of the tubular membrane, as shown by Fig. 3 (A-E), Fig. 3 (F) shows that long NPs, at low values of $\mu$, are tilted with respect to the tubule's principal axis. The effects of curvature mismatch and NP's arclength on its tilt will be quantified and discussed in more detail in Section III B.

We found that the kinetics of binding of a NP to the membrane proceeds through two or three steps, as shown by Fig. 5. Fig. 5 (A), which corresponds to the case of $\mu \approx 2.3$, shows that initially, the NP adheres to the membrane via its two ends. This upright mode of adhesion is associated with a low binding energy and very weak deformation of the membrane, and is characterized by a high transverse and longitudinal diffusivity of the NP on the membrane. The upright adhesion mode is then abruptly followed by a sidewise adhesion mode, shown by the middle snapshot of Fig. 5 (A). This mode is also associated with weak deformation of the membrane. Interestingly, the NP's end-to-end vector, $\overrightarrow{PR}$, in this adhesion mode is mostly perpendicular to the tubule's axis. The NP is slightly tilted in this mode, i.e., the plane containing the NP points $P$, $Q$ and $R$ (defined in Fig. 2) is not parallel to the tubule's axis. This mode of adhesion allows the NP to maximize contact with the tubule while maintaining weak deformation of the tubule. The sidewise adhesion mode may be counterintuitive since the interaction between the $p$-beads of the NP and the lipid bead $h$-beads is fully repulsive. However, since the range

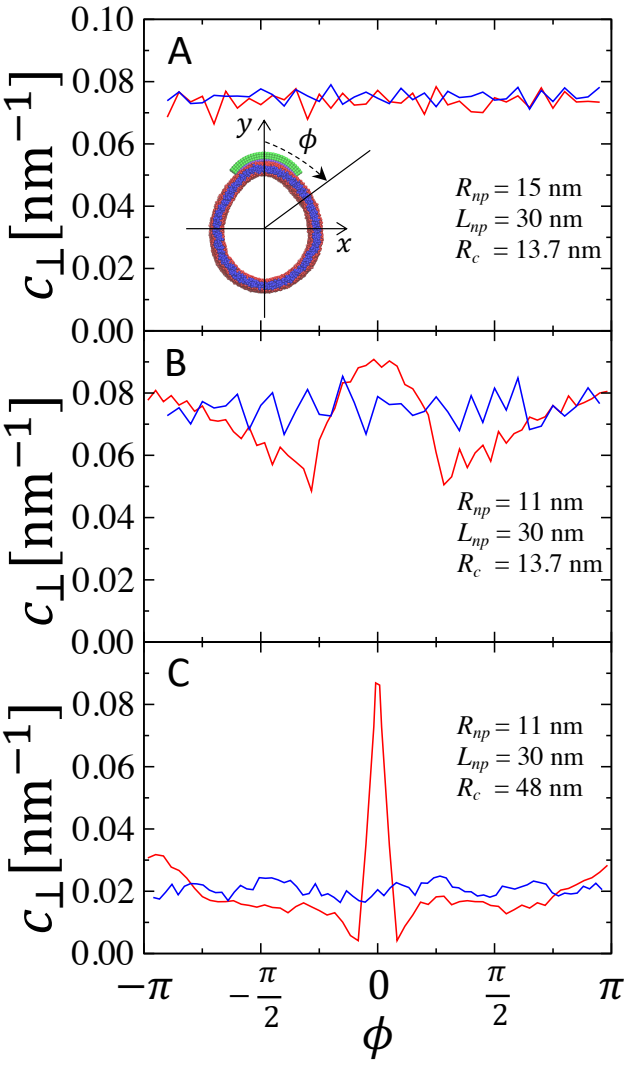


FIG. 4: Transverse curvature, $c_\perp$ versus the polar angle $\phi$, defined in the inset of (A). Blue and red curves correspond to the case where the NP is unbound and unbound, respectively. The bound state and unbound states correspond to adhesion strength right after and before the adhesion threshold, respectively. (A) corresponds to a case of weak mismatch $R_{np} = 15$ nm, $L_{np} = 30$ nm and $R_c = 13.7$ nm. (B) corresponds to a case of moderate mismatch $R_{np} = 11$ nm, $L_{np} = 30$ nm and $R_c = 13.7$ nm. (A) corresponds to a case of strong mismatch $R_{np} = 15$ nm, $L_{np} = 30$ nm and $R_c = 13.7$ nm.

of this interaction is shorter than that between the $n$-beads and the $h$-beads, strong enough attractive $n-h$ interaction can offset the repulsive $p-h$ interaction in the sidewise adhesion mode. A sidewise adhesion mode with the end-to-end $\overrightarrow{PR}$-vector that is parallel to the tubule's axis is not favorable since this would lead to more contacts between the $p$-beads and the $h$-beads, and therefore a net repulsive interaction between the NP and the membrane that is too high to be offset by the net attractive interaction between the $n$-beads and the $h$-beads. Increasing the strength of the repulsive interaction between the $n$-beads and $h$-beads makes the sidewise adhesion mode less favorable as an intermediate state. Frost *et al.* [32] observed that F-BAR domain proteins can bind sidewise if the to membrane is too rigid. This adhesion mode was later confirmed by both atomistic and coarse-grained simulations [38]. Finally, the NP then abruptly fully adheres to the membrane through its concave side, as shown by the right snapshot in Fig. 5 (A). In contrast to the two previous adhesion modes, the final mode of adhesion is associated with the highest amount of membrane deformation.

Fig. 5 (B) shows that at higher curvature mismatch, $\mu \approx 4.5$, the binding of the NP proceeds first through the upright mode, then followed directly by the full adhesion mode, bypassing the sidewise adhesion mode. This is due to the fact that due to the flatter nature of the tubule, for high $\mu$, a sidewise adhesion mode would require the NP's plane containing the points $P$, $Q$ and $R$ to be almost parallel to the tubule's axis, leading to more unfavorable contact between the lipid head beads and the NP's $p$-beads than for the case of low values of $\mu$.

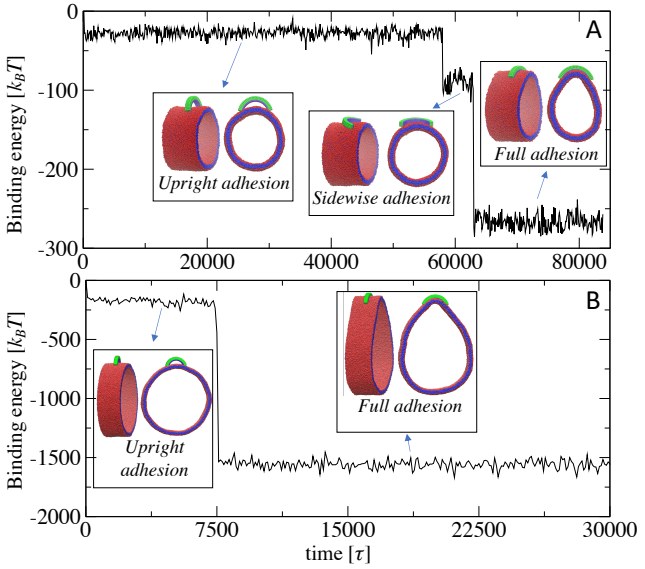


FIG. 5: (A) The binding energy vs time for the case of a NP with $R_{np} = 11$ nm, $L_{np} = 30$ nm, on a tubular membrane of radius $R_c = 25.2$ nm at the adhesion strength $\xi = 1.5\epsilon$. Also shown are typical configurations depicting the three modes of adhesion, corresponding to the upright adhesion mode, sidewise adhesion mode and full adhesion mode. (B) Same as (A) for a NP with same radius of curvature and arclength on a tubular membrane with $R_c = 48$ nm and at the adhesion strength $\xi = 2.4\epsilon$.

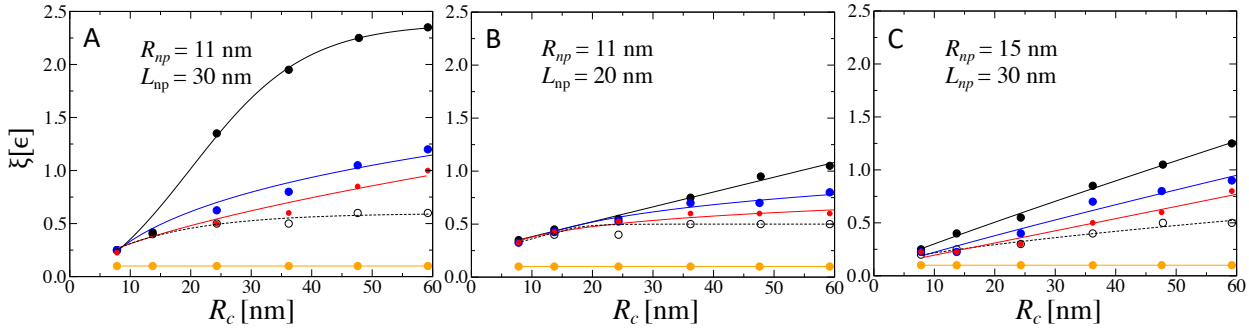


FIG. 6: Binding/unbinding phase diagrams in terms of radius of the tubular membrane, $R_c$, and adhesion strength, $\xi$, for $(R_{np}, L_{np}) = (11\text{ nm}, 30\text{ nm})$ (A), $(R_{np}, L_{np}) = (11\text{ nm}, 20\text{ nm})$ (B), and $(R_{np}, L_{np}) = (15\text{ nm}, 30\text{ nm})$ (C). Solid black circles correspond to the binding threshold, obtained from upward annealing with respect to $\xi$. Open black circles correspond to the unbinding threshold, obtained from downward annealing scans. Orange circles represent the binding threshold for the case of flat NPs (i.e. for $R_{np} = \infty$). The blue circles represent the binding threshold of a second NP to the membrane. Red circles correspond to the binding/unbinding transition as obtained from free energy calculation (see text for explanation). Solid lines are guides to the eye.

### A. Binding/Unbinding Transition of a Single NP

The binding and unbinding thresholds, are obtained from upward and downward annealing scan simulations, respectively, with respect to the adhesion strength $\xi$, for different values of the radius of the tubular membrane $R_c$. Fig. 6 shows the binding and unbinding thresholds (solid and open black circles, respectively) for three combinations of $(R_{np}, L_{np})$ corresponding to $(11\text{ nm}, 30\text{ nm})$ (Fig. 6 (A)), $(11\text{ nm}, 20\text{ nm})$ (Fig. 6 (B)) and $(15\text{ nm}, 30\text{ nm})$ (Fig. 6 (C)). We emphasize that since the upright and sidewise adhesion modes (see Fig. 5) appear only as intermediate states, we use the full adhesion mode to define binding of the NP to the membrane. The results in Fig. 6 are obtained from simulations on tubular membranes with $L_z = 30$ nm. We did few simulations on tubes with $L_z = 60$ nm and found identical results. The solid black symbols, in Fig. 6, correspond to the binding adhesion strength, $\xi_b$, and are obtained from upward annealing scans with respect to $\xi$. The open black circles correspond to the unbinding adhesion strength, $\xi_u$, and are obtained from downward annealing scans. Fig. 6 shows that for any $R_c \gtrsim R_{np}$, $\xi_b > \xi_u$, indicating that the binding/unbinding transition is discontinuous, and that there exists an energy barrier against the binding of the NPs to the tubular membrane. We note that the binding energy per unit of area, corresponding to about $2k_BT/\text{ nm}^2$ for the case of the 25-nm tubule and $11k_BT/\text{ nm}^2$ for the case of the 48-nm tubule, is inline with estimated binding energies of BAR-domains of about $5k_BT/\text{ nm}^2$ [55, 56].

Fig. 6 also shows that, for a given NP's curvature, both binding and unbinding thresholds increase with $R_c$. Furthermore, Fig. 6 shows that $\xi_b - \xi_u$ increases with increasing $R_c$, implying an increase in the energy barrier against binding as $\mu$ is increased. A comparison between Fig. 6 (A) and (C) shows that for a given $R_c$, $\xi_b$ increases with increasing the NP's curvature. Therefore, the binding adhesion strength threshold is increased with increasing curvature mismatch $\mu$.

The discontinuous nature of the binding-unbinding transition of anisotropically curved NPs can be inferred from the inspection of the tubule's conformation right after full binding of the NP. Fig. 7 shows that right after full binding, apart from the portion of the membrane bound to the NP, the tubule's cross-section remains mostly circular. The difference between the curvature energy of this intermediate state and that before binding is approximately given by

$$\Delta F_c = \frac{\kappa l}{2R_c^2}\left[L_{np}\left(\mu^2 - \frac{R_c^2}{\tilde{R_c}^2}\right) + 2\pi R_c\left(\frac{R_c^2}{\tilde{R_c}^2} - 1\right)\right], \quad (10)$$

where $\kappa$ is the membrane's bending modulus and $l$ is the length of the tubule along the $z$-axis. Here, the defor-

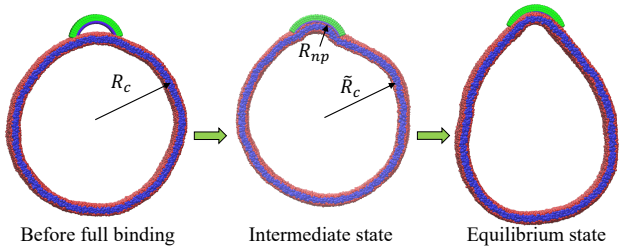


FIG. 7: Snapshots of the tubule, in the case of $R_{np} = 11$ nm, $L_{np} = 30$ nm, $R_c = 48$ nm and $\xi = 2.4\epsilon$, before full binding (left), right after full binding (center) and at equilibrium (right).

mation is assumed to extend throughout the $z$-axis, as is the case in our simulations. In the case where $\mu > 1$, $R_{np} < \tilde{R}_c < R_c$. As a result, $\Delta F_c$ increases as either $L_{np}$ or $\mu$ is increased, implying an increase in the energy barrier with increasing $\mu$ or $L_{np}$, and therefore a widening of the gap between the binding and unbinding thresholds, in agreement with Fig. 6. This analysis also agrees with the fact that for $\mu \approx 1$, the binding and unbinding thresholds are practically identical, in agreement with Fig. 6.

We also performed simulations of flat NPs ($1/R_{np} = 0$) and found that they bind in such a way that they lie parallel to the tubule's axis. Furthermore, we found that the binding and unbinding transitions of flat NPs are identical as shown by the orange data in the phase diagrams of Fig. 6, implying a reversible nature of the binding transition of flat NPs. As in the case of curved NPs, the binding of flat NPs is also a first-order transition since the contact area between the NP and the membrane increases discontinuously from 0 to the a finite value corresponding to the area of the face of the NP that interacts attractively with the membrane. Therefore, the reversibility of this transition implies that the energy barrier between the unbound and bound states of flat NPs is about or weaker than the thermal energy. Fig. 6 also shows that unlike curved NPs, the binding/unbinding transition of flat NPs is independent of the curvature of the tubule or length of the NP, and lower than the binding and unbinding transitions of the crescent NPs.

We also inferred the binding of a second NP on the tubule by performing upward annealing simulations of an unbound NP and a tubular membrane with an already bound NP. The binding threshold of the second NP is shown by the blue data in Fig. 6 (A-C). This figure shows that the binding energy threshold of the second NP is weaker than that of the first NP. We also found that the second NP binds at a location near the first NP, where a local curvature of the membrane has already been generated by the first NP. The adhesion of the second NP is therefore mediated by curvature sensing which is energetically less taxing than the adhesion of the first NP, which requires curvature generation.

To validate the binding/unbinding transitions discussed earlier, we calculated the free energy of the composite membrane-NP system given by

$$\mathcal{F} = \mathcal{F}_{\rm adh} + \mathcal{F}_{\rm curv}, \tag{11}$$

where $\mathcal{F}_{\rm adh}$ is the net potential energy due to interactions between the NP and the membrane. $\mathcal{F}_{\rm curv}$, is estimated using the Helfrich Hamiltonian [57] with a local Monge representation following a method we introduced earlier [23]. This approach does not account for the membrane conformational entropic contributions, while only partially accounts for the lipids conformational entropy. As such, this approach is a saddle-point approximation. In Eq. (11), we neglect the contribution arising from the the spontaneous curvature which can be induced from the redistribution of the lipids in the inner and outer leaflets of the tubules [58]. Furthermore, since the volume of a tubule in our model is not constrained, the area of the tubule freely adjusts to a value that minimizes the surface energy. Hence, a tension term is also not accounted for in Eq. (11). The results from this approach are shown by the red data in the phase diagrams of Fig. 6. The free energy calculations therefore predict an equilibrium binding/unbinding phase transition that nicely lies between the non-equilibrium binding and unbinding transitions that are respectively obtained from upward and downward annealing scans with respect to $\xi$.

### B. Modes of NPs Adhesion

We have seen earlier that when the curvature mismatch $\mu > 1$, the NP's end-to-end vector lies perpendicularly to the axis of the tubular membrane, as in the case of Fig. 3 (A-E). However, NPs are tilted with respect to the tubule's axis for $\mu < 1$ as in the case of Fig. 3 (F). We characterize the NP's tilt by the angle, $\theta$, between the axis of the tubular membrane and the axis perpendicular to the plane containing the three points, $P$, $Q$ and $R$, on the NP, as indicated in Fig. 8 (A). $\theta = 0$ therefore corresponds to an NP lying perpendicularly to the tubule.

The tilt angle vs the tubule's radius is depicted in Fig. 8 (B) for the cases of $R_{np} = 15$ and 19 nm, both with $L_{np} = 30$ nm and at the adhesion strength $\xi = 1\epsilon$. This figure shows that the tilt angle is indeed close to 0 when $R_c > R_{np}$, and that it increases monotonically with decreasing $R_c$. Fig. 8 (B) also shows that for a given $R_c$, the average value of the tilt angle increases with increasing NP's radius of curvature. The reason why the tilt angle remains finite even for large values of $R_c$ is due to fluctuations and the fact that by definition $0 \leq \theta \leq 90^o$. Interestingly, Fig. 8 (C) shows that the tilt angle depends only on the mismatch parameter, $\mu$, for a given $L_{np}$.

A rough estimation of the tilt angle, in the case of $\mu < 1$, can be obtained from the following purely geometric argument, which assumes that the tubule's geometry remains cylindrical when the NP adheres at some tilt. A maximum contact between the NP and the membrane is therefore achieved if the NP tilts at an angle such that its radius of curvature is equal to the maximum radius of curvature, $R_{max}$, of the ellipse resulting from the intersection between the plane containing points $P$, $Q$ and $R$ belonging to the NP, and the tubule's cylinder, as shown by Fig. 8 (A),

$$R_{np} = R_{max} = b^2/a, \tag{12}$$

where $a = R_c$ is the length of the semi-minor axis of the ellipse, and $b = R_c/\sin\theta$ is the length of the semi-major axis of the ellipse. This leads to a tilt angle

$$\theta = \cos^{-1}\sqrt{\mu}. \tag{13}$$

We note that the assumption in this argument that the tubule remains cylindrical implies that the NP cannot

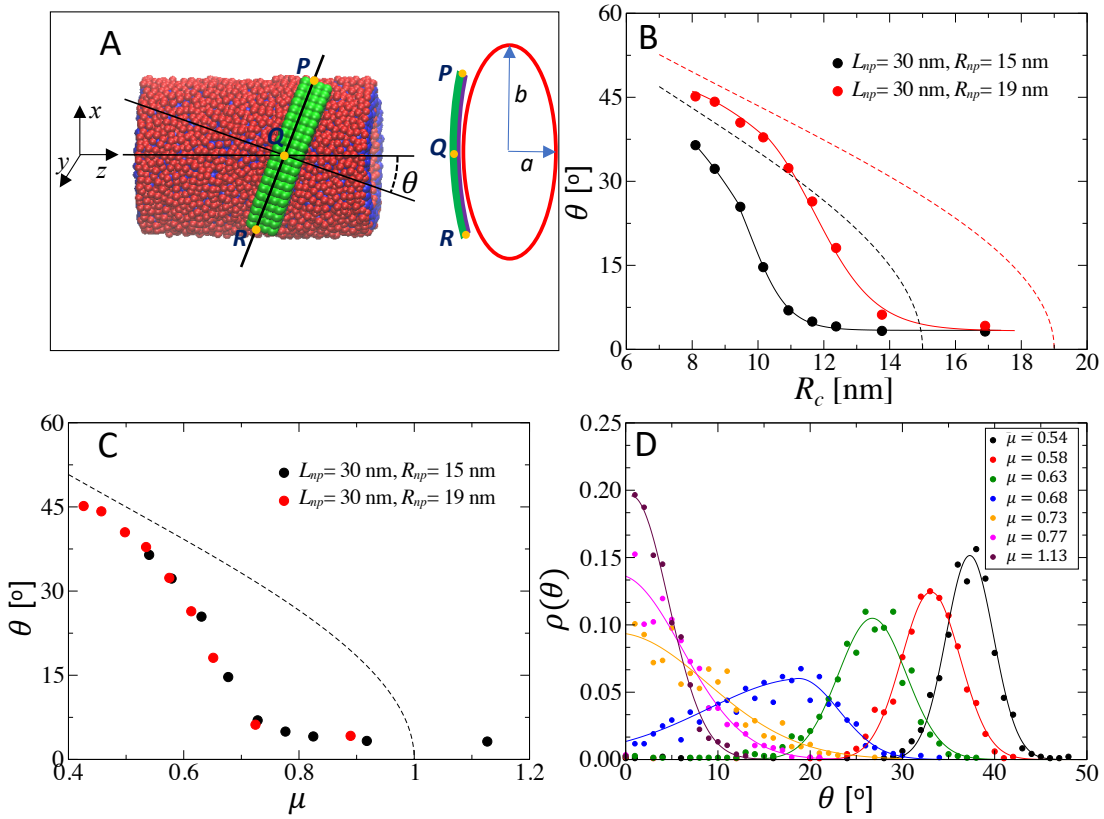


FIG. 8: (A) Left: A configuration showing a NP adhered to a lipid tubule with a tilt angle $\theta$. Right: The ellipse resulting from the intersection of the plane containing the three points $P$, $Q$ and $R$, which belong to the NP, and the cylinder of radius $R_c$. $a$ and $b$ are the semi-minor and semi-major axes of the ellipse, respectively. (B) Tilt angle for the case of NPs with $R_{np} = 15$ nm (black points) and 19 nm (red points) at $\xi = 1\epsilon$. Both NPs have same arc length $L_{np} = 30$ nm. The dashed lines are obtained from Eq. (13). (C) Tilt angle vs curvature mismatch $\mu$ for the case of $L_{np} = 30$ nm. Symbols are the same as in (B) and the dashed line corresponds to Eq. (13). (D) Normalized distributions of the tilt angle for the case of NPs with $R_{np} = 15$ nm and $L_{np} = 30$ nm, at different values of the radius of the tubular membrane.

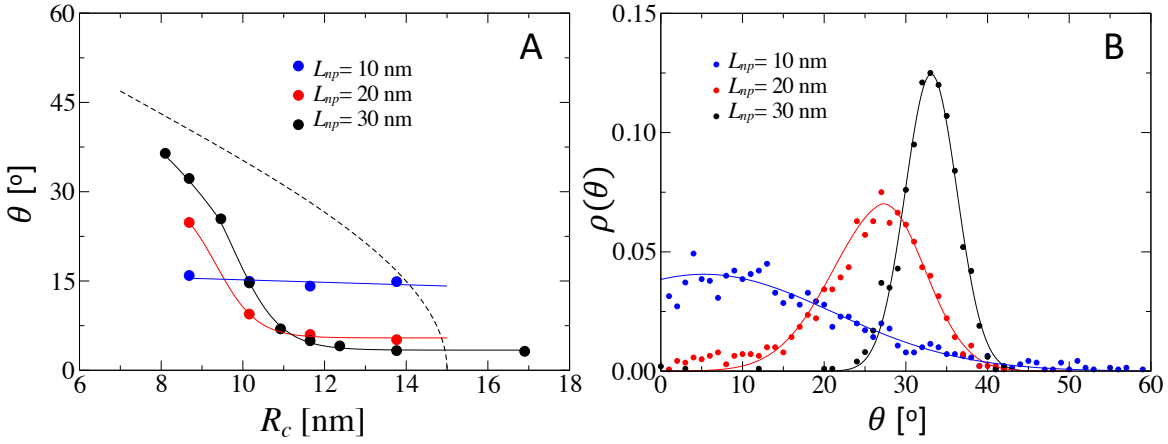


FIG. 9: (A) Tilt angle vs radius of the tubular membrane for the case of $R_{np} = 15$ nm. Data shown correspond to $L_{np} = 30$ nm (black), $L_{np} = 20$ nm (red) and $L_{np} = 10$ nm (blue). The dashed line corresponds to Eq. (13). (B) Normalized distributions of the tilt angle for systems shown in (A) in the case of $R_c = 8.68$ nm.

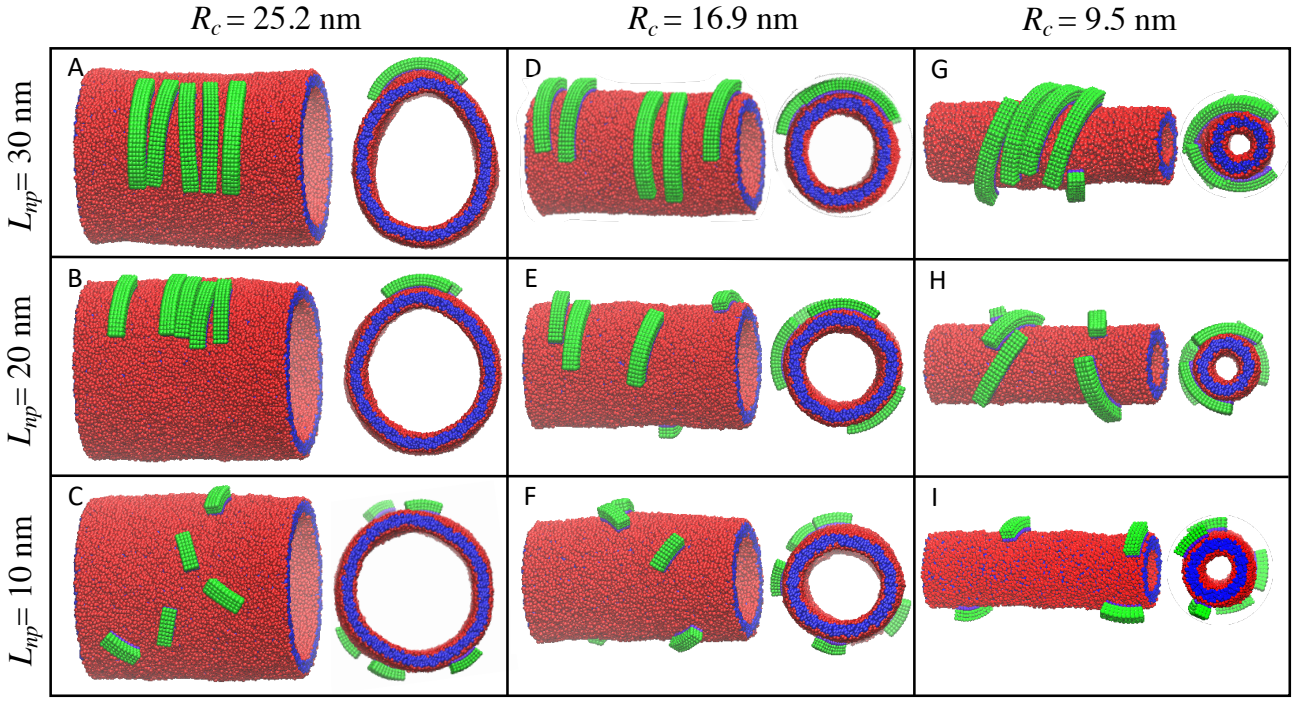


FIG. 10: Configuration snapshots of 5 NPs with radius of curvature $R_{np} = 15$ nm with different arclengths on tubular membranes with different radii. Configurations on the left, middle and right rows correspond to curvature mismatch $\mu = 1.68$, 1.13 and 0.633 respectively. The configurations are obtained from simulations at $\xi = 0.6\epsilon$.

fully adhere to the tubule, since the NP has a constant curvature whereas the bisecting ellipse has varying curvature, as shown by Fig. 8 (A). Nevertheless, Fig. 8 (B) and (C) show that the tilt angle as predicted by this geometric argument is in qualitative agreement with the simulations.

A major difference between the numerical results and the geometric argument, as shown by Fig. 8 (C), is that the NPs are substantially tilted only for $\mu \lesssim \mu^* \approx 0.7$ (corresponding roughly to the inflection point of the graph of the tilt angle versus $\mu$ in Fig. 7(C)) in the case of $L_{np} = 30$ nm. To understand why the tilt angle remains small even when $\mu$ is slightly lower than 1, we extracted the distribution of the tilt angle, $\rho(\theta)$, for different values of $\mu$. Fig. 8 (D) shows the tilt angle distributions for the case of $R_{np} = 15$ nm and $L_{np} = 30$ nm for different values of $R_c$. This figure shows that $\rho(\theta)$ is peaked at $\theta = 0$ for $\mu > \mu^*$, implying that for this range of $\mu$, non-tilted configurations of the NP are most probable, albeit with a large amount of fluctuations around $\theta = 0$.The distributions become peaked at a finite values of $\theta$ only for $\mu \lesssim \mu^*$, and the amount of fluctuations in the tilt angle decreases with decreasing $\mu$.

We now turn to the effect of the NP's arclength on its mode of binding. Fig. 9 (A) depicts the tilt angle vs the radius of the tubular membrane for NPs with radius of curvature $R_{np} = 15$ nm and three values of the arc length, $L_{np} = 10$, 20, and 30 nm. Fig. 9 (B) shows the tilt angle distributions of these systems for the case of $R_c = 8.68$ nm ($\mu = 0.58$). This figure shows that the distributions for $L_{np} = 20$ and 30 nm are peaked at finite values of $\theta$. However, for the case of $L_{np} = 10$ nm, the distribution is peaked at $\theta \approx 0$. This implies that short NPs are in general non-tilted even for low values of $\mu$. Fig. 9 (A) shows that as the NP's arclength is decreased, the crossover radius of the tubule between the tilted and non-tilted configurations of the NP, is shifted to lower values. This implies that $\mu^*$ decreases with decreasing $L_{np}$. We note the crossover $\mu^*$ is not observed for the shortest NPs ($L_{np} = 10$ nm), since this would require very thin tubules which cannot be simulated while maintaining their stability. Fig. 9 (B) also shows that the spread of the distributions increases with decreasing NP's arclength. This implies that the degree of NP's tilt is the result of a competition between the positional entropy of the NP on the tubule and the binding energy whose absolute value decreases with decreasing NP's arclength.

### C. Self-Assembly of NPs on Tubular Membranes

We now turn to the self-assembly of many NPs on tubular membranes. Here we focus on the case of relatively weak adhesion strength, corresponding to $\xi = 0.6\epsilon$. Fig. 10 shows snapshots of 5 NPs with $R_{np} = 15$ nm and three values of $L_{np}$ on tubular membranes with radius of curvature $R_c = 25.2$, 16.9 and 9.5 nm. The results are obtained from simulations of tubular membranes of

length $L_z = 62$ nm. The self-assembly of the NPs is quantified in Fig. 11 through scatterplots of the separation between the centers of mass of the two NPs along the $z$-axis, $\Delta z$, and their angular separation, $\Delta\phi$ (as schematically defined in the inset of Fig. 11 (A)).

Fig. 10 (A-C), which correspond to the case of $R_c = 25.2$ nm and $\mu = 1.68$ for different values of the NP's arclength, show that the arrangement of the NPs on the tubular membrane depends on their arclength. Longest NPs ($L_{np} = 30$ nm) self-assemble into linear chains along the $z$-axis and are arranged side-by-side. The corresponding scatterplot shown in Fig. 11 (A) shows that both $\Delta\phi$ and $\Delta z$ are indeed small. This self-assembly is caused by the fact that, in this case, the NPs cause an appreciable curvature deformation of the tubule, thereby limiting NPs to be located in the most curved region of the tubule.

For $L_{np} = 20$ nm, both Fig. 10 (B) and Fig. 11 (B) show results similar to the case of $L_{np} = 30$ nm, although in this case, $\Delta z$ extends to higher values. This must be due to the fact that the amount of tubule's deformation in this case is less than that in the case of $L_{np} = 30$ nm and the tilt angle distribution widens with decreasing NPs arclength, as discussed earlier, leading to increased steric repulsion between the NPs. Both Fig. 10 (C) and Fig. 11 (C) show that the shortest NPs ($L_{np} = 10$ nm) are distributed uniformly on the tubule. This is due to the fact that the shortest NPs do not cause much deformation of the tubule.

Fig. 10 (D-F) show that as $\mu$ is decreased to 1.13, the NPs are more distributed uniformly on the tubule, both in terms of separation angle and distance. This is expected since, as we have seen earlier, the amount of morphological deformation of the tubule caused by the NP decreases as $\mu$ approaches 1.

Fig. 10 (G-I) show that as $\mu$ is further decreased to 0.63, NPs with $L_{np} = 30$ nm are relatively close to each other, but the separation angle is more widely distributed as compared to the case of $\mu = 1.68$, as demonstrated by the snapshot of Fig. 10 (G) and by the scatterplot of Fig. 12 (A). However, as the arclength of the NPs is decreased, the NPs distribution on the tubule becomes more uniform, as demonstrated by the snapshots of Fig. 10 (H and I) and by the scatterplot of Fig. 12 (B). The proximity of the NPs with $L_{np} = 30$ nm along the $z$-axis is attributed to a localized deformation of the tubule along the $z$-axis into a slightly flattened shape. As $L_{np}$ is decreased, the amount of tubule's deformation is decreased, leading to the more uniform distribution of the NPs. The results above show that the higher is the NPs arclength and mismatch between the NPs curvature and that of the tubule, the more prone they are to self-assemble into chains on the tubule.

## IV. SUMMARY AND CONCLUSIONS

In summary, we presented in this article results of a detailed systematic molecular dynamics study, based on an implicit-solvent model, of the interaction between tubular lipid membranes and crescent-shaped NPs, that interact with the membrane through their concave side. Crescent-shaped NPs are either unbound or completely bound to the lipid membrane. In the bound state, the concave surface of the NP is completely apposed to the outer surface of the lipid membrane. Using annealing scans with respect to the adhesive energy, we found that the binding transition of the NPs is highly first-order,

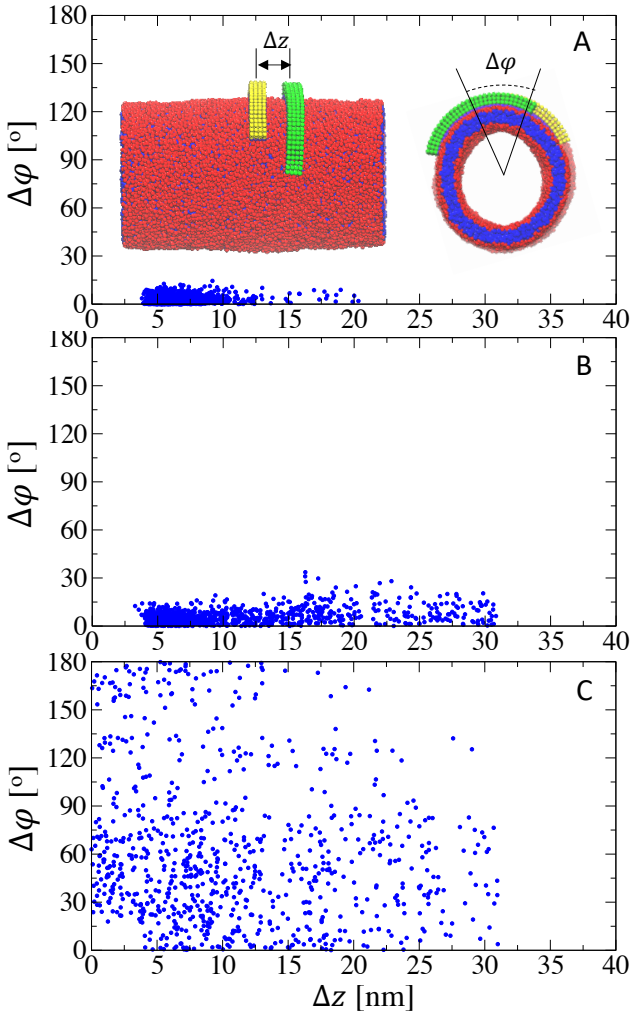


FIG. 11: Scatter plot of the separation angle between two neighboring NPs, $\Delta\phi$, and separation distance along the $z$-axis, $\Delta z$, for the case of NPs with radius of curvature $R_{np} = 15$ nm on tubular membranes with $R_c = 25.2$ nm at the adhesion strength $\xi = 0.6\epsilon$. (A), (B) and (C) correspond to NPs with arclength $L_{np} = 30$, 20 and 10 nm, respectively. The definitions of $\Delta\phi$ and $\Delta z$ are illustrated in the inset snapshots of (A).

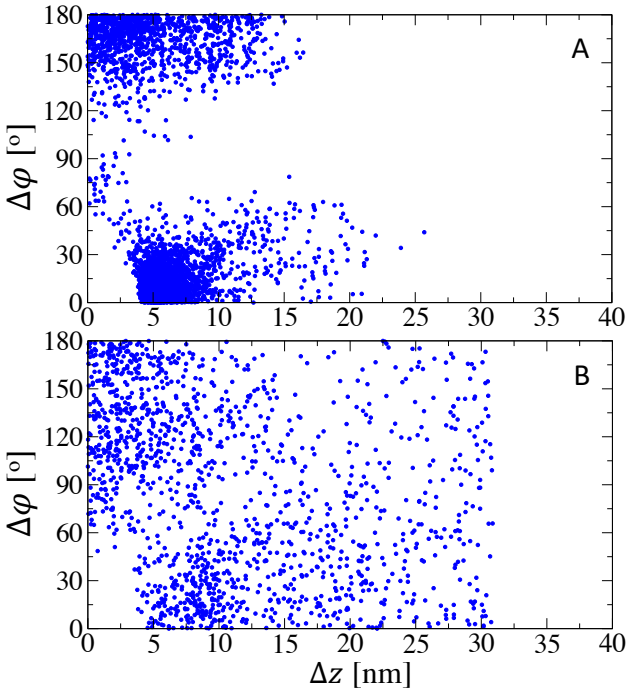


FIG. 12: Scatter plot of $\Delta\phi$ vs $\Delta z$ for the case of $R_{np} = 15$ nm and $R_c = 9.5$ nm at the adhesion strength $\xi = 0.6\epsilon$. (A) and (B) correspond to $L_{np} = 30$ nm and 20 nm, respectively.

with the binding adhesive energy, per unit area, being higher than the unbinding adhesive energy per unit area. We also found that both binding and unbinding adhesion thresholds increase with increasing NPs arclength, $L_{NP}$, or curvature mismatch, defined as $\mu = R_c/R_{np}$ where $R_{np}$ and $R_c$ are the radii of curvature of the NP and tubule, respectively. Furthermore, the difference between these energies increases with $\mu$ or $L_{NP}$. This implies that the affinity of these NPs to bind to lipid membranes diminishes with increasing $\mu$ or the NPs' arclength. The discontinuous nature of the binding transition is due to the fact that the binding of crescent-shaped NPs on tubular membranes proceeds through intermediate states with high curvature energy that can only be overcome for high enough adhesion energy. We also found, that an additional NP binds at a location vicinal to the first one, where a friendly curvature has already been generated by the first NP. This leads to a lower adhesion threshold of additional NPs.

Much of our understanding of the interaction between NPs and lipid membranes is based on studies of NPs with various geometries that adhere to lipid membranes through their convex surfaces. In these cases, the membrane wraps the NPs to a degree that increases with increasing adhesion strength or the NPs mean radius of curvature. The increase in the degree of wrapping of such NPs by the membrane often exhibits a first order transition, with an energy barrier that increases with increasing the degree of the NPs' anisotropy [26]. A major difference between the adhesion transition of these NPs and crescent-shaped NPs is that the the latter do not partially bind to lipid membranes, and the transition is between unbound and completely bound states.

The crescent-shaped NPs considered in the present study are reminiscent of both F-BAR and N-BAR domain proteins, which also adhere to lipid membranes through their concave surfaces. The NPs in our study are however considerably simpler in structure than BAR domain proteins, whose binding to the lipid membrane is often aided by amphipathic residues that insert in the hydrophobic core of the membrane.

The binding mode of the crescent-shaped NPs depends on both the curvature mismatch and their arclength. NPs with high curvature mismatch lie perpendicularly to the axis of the tubule for $\mu > 1$. However for low mismatch values $\mu \lesssim \mu^* < 1$, where $\mu^*$ increases with increasing $L_{np}$, the NPs are tilted with respect to the tubule's axis, with the tilt angle that increases with decreasing $\mu$. Interestingly, we found that in the range of curvature mismatch $\mu^* \lesssim \mu < 1$, non-tilted configurations of the NPs remain most probable, as in the case of $\mu > 1$, albeit with an increased amount of fluctuations.

Finally, we also investigated the self-assembly of the crescent NPs on tubular membranes, and found that they self-assemble into chains when both curvature mismatch and NPs arclength are high, in agreement with our prior study [52]. However for $\mu \approx 1$ or low values of arclength, the NPs distribute more uniformly on the tubule. The self-assembly of these NPs is mediated by the membrane curvature. Experiments have shown that various types of BAR-domain proteins organize into well-ordered structures on lipid membranes [59]. However, there is hint that protein-protein interactions play a major role on these self-assemblies [32, 59]. Computational studies of coarse-grained models, where the main effect of the BAR-domain proteins is taken to be induction of a local spontaneous curvature of the membrane while neglecting many microscopic details, have shown that the proteins self-assemble on the membrane [39, 45, 46, 49] in agreement with our results. Due to the complex structure of BAR-domain proteins, it is difficult to determine the contribution of protein-protein interaction to their self-assembly on lipid membranes. Therefore, It would be very desirable to test the present results experimentally through simple crescent-shaped NPs. Recent advances in nanomaterials fabrication which allow for the synthesis of crescent-shaped NPs with tunable dimensions and properties [60–63] should make this possible.

**Acknowledgements**

This work was supported by a grant from the National Science Foundation (DMR-1931837). All simulations were performed on computers of the High Performance Computing Facility of the University of Memphis. All snapshots in this article were generated using VMD version 1.9.3 [64].

[1] J.N. Anker, W. P. Hall, O. Lyandres, N.C. Shah, J. Zhao, and R.P. Van Duyne, Nat. Mat., 2008, **7**, 442-453.
[2] K. Wang, F.M. Kievit, and M. Zhang, Pharmacol. Res., 2016, **114**, 56-66.
[3] A. J. Mieszawska, W.J.M. Mulder, Z.A. Fayad, and D.P. Cormode, Mol. Pharm., 2013, **10**, 831-847.
[4] T. Sun, Y.S. Zhang, B. Pang, D.C. Hyun, M. Yang, and Y. Xia, Ang. Chem., 2014, **53**, 12320-12364.
[5] A.E. Nel, L. Mädler, D. Velegol, T. Xia, E.M.V. Hoek, P. Somasundaran, F. Klaessig, V. Castranova, and M. Thompson Nat. Mat., 2009, **8**, 543-557.
[6] E.A. Perigo, G. Hemery, O. Sandre, D. Ortega, E. Garaio, F. Plazaola, and F.J. Teran, Appl. Phys. Rev., 2015, **2**, 041302.
[7] A.V. Singh, P. Laux, A. Luch, C. Sudrik, S Wiehr, A.M. Wild, G. Santomauro, J. Bill, and M. Sitti, Toxic. Mech. Meth., 2019, **29**, 378-387.
[8] S.E.A. Gratton, P.A. Ropp, P.D. Pohlhaus, J.C. Luft, V.J. Madden, M.E. Napier, and J.M. DeSimone, Proc. Natl. Acad. Sci. U. S. A., 2008, **105**, 11613-11618.
[9] S. Dasgupta, T. Auth, and G. Gompper, Nano Lett., 2014, **14**, 687-693.
[10] C. Huang, Y. Zhang, H. Yuan, H. Gao, and S. Zhang, Nano Lett., 2013, **13**, 4546-4550.
[11] J. Agudo-Canalejo and R. Lipowsky, ACS Nano, 2015, **9**, 3704-3720.
[12] J. Agudo-Canalejo and R. Lipowsky, Nano Lett., 2015, **15**, 7168-7173.
[13] A.H. Bahrami, R. Lipowsky, and T. Weikl, Soft Matter, 2016, **12**, 581-587.
[14] Q. Yu, S. Othman, S. Dasgupta, T. Auth, and G. Gompper, Nanoscale, 2018, **10**, 6445-6458.
[15] M. Deserno and W. M. Gelbart, J. Phys. Chem. B, 2002, **106**, 5543-5552.
[16] M. Deserno and T. Bickel, Europhys. Lett., 2003, **62**, 767-773.
[17] T. Ruiz-Herrero, E. Velasco, and M. F. Hagan, J. Phys. Chem. B, 2012, **116**, 9595-9603.
[18] A. Saric and A. Cacciuto, Phys. Rev. Lett., 2012, **109**, 188101.
[19] A. Saric and A. Cacciuto, Phys. Rev. Lett., 2012, **108**, 118101.
[20] M. Raatz, R. Lipowsky, and T.R. Weikl, Soft Matter, 2014, **10**, 3570-3577.
[21] E. J. Spangler, S. Upreti, and M. Laradji, J. Chem. Phys., 2016, **144**, 044901.
[22] K. Xiong, J. Zhao, D. Yang, Q. Cheng, J Wang, and H. Ji, Soft Matter, 2017, **13**, 4644-4652.
[23] E.J. Spangler, P.B. Sunil Kumar, and M. Laradji, Soft Matter, 2018, **14**, 5019-5030.
[24] E.J. Spangler and M. Laradji, J. Chem. Phys., 2020, **152**, 104902.
[25] A.H. Bahrami, Soft Matter, 2013, **9**, 8642-8646.
[26] S. Dasgupta, T. Auth, and G. Gompper, Soft Matter, 2013, **9**, 5473-5482.
[27] B.J. Reynwar, G. Illya, V.A. Harmandaris, M.M. Müller, K. Kremer, and M. Deserno, Nature, 2007, **447**, 461-464.
[28] A.H. Bahrami and T.R. Weikl, Nano Lett, 2018, **18**, 1259-1263.
[29] A. Frost, V.M. Unger, and P. De Camilli, Cell, 2009, **137**, 191-196.
[30] C. Mim and V.M. Unger, Trends Biochem. Sci., 2012, **37**, 526-533.
[31] B.J. Peter, H.M. Kent, I.G. Mills, Y. Vallis, P.J.G. Butler, P.R. Evans, and H.T. McMahon, Science, 2004, **303**, 495-499.
[32] A. Frost, R. Perera, A. Roux, K. Spasov, O. Destaing, E.H. Egelman, P. De Camilli, and V.M. Unger, Cell, 2008, **132**, 807-817.
[33] P.K. Mattila, A. Pykäläinen, J. Saarikangas, V.O. Paavilainenm H. Vihinen, E. Jokitalo, and P. Lappalainen, J. Cell Biol., 2007, **176**, 953-964.
[34] M. Simunovic, G.A. Voth, A. Callan-Jones, and P. Bassereau, Trends Cell Biol., 2015, **25**, 780-792.
[35] A.J. Sodt and R.W. Pastor, Biophys. J., 2014, **106**, 1958-1969.
[36] K. Takemura, K. Hanawa-Suetsugu, S. Suetsugu, and A. Kitao, Sci. Rep., 2017, **7**, 6808.
[37] A. Arkhipov, Y. Yin, and K. Schulten, Biophys. J., 2009, **97**, 2727-2735.
[38] H. Yu and K. Schulten, PLoS Comput. Biol., 2013, **9**, e1002892.
[39] M. Simunovic, A. Srivastava, and G.A. Voth, Proc. Natl. Acad. Sci. U. S. A., 2013, **110**, 20396-20401.
[40] M. Simunovic and G.A. Voth, Nat. Commun., 2015, **6**, 7219.
[41] M. Simunovic, A. Saric, J.M. Henderson, K.Y.C. Lee, and G.A. Voth, ACS Cent. Sci., 2017, **3**, 1246-1253.
[42] M.I. Mahmood, H. Noguchi, and K.Okazaki, Sci. Rep., 2019, **9**, 14557.
[43] Y. Yin, A. Arkhipov, and K. Schulten, Structure, 2009, **17**, 882-892.
[44] T.V.S. Krishnan, S.L. Das, and P.B. Sunil Kumar, Soft Matter, 2019, **15**, 2071-2080.
[45] N. Ramakrishnan, J.H. Ipsen, and P.B. Sunil Kumar, Soft Matter, 2012, **8**, 3058-3061.
[46] N. Ramakrishnan, J.H. Ipsen, and P.B. Sunil Kumar, Biophys. J., 2013, **104**, 1018-1028.
[47] N. Ramakrishnan, M. Rao, J.H. Ipsen, and P.B. Sunil Kumar, Soft Matter, 2015, **11**, 2387-2393.
[48] T.V.S. Krishnan, S.L. Das, and P.B. Sunil Kumar, Pramana - J. Phys., 2020, **94**, 47.
[49] H. Noguchi, J. Chem. Phys., 2015, **143**, 243109.
[50] H. Noguchi, Sci. Rep., 2016, **6**, 20935.
[51] M. Laradji, P.B. Sunil Kumar, and E.J. Spangler, J. Phys. D: Appl. Phys., 2016, **49**, 293001.
[52] A.D. Olinger, E.J. Spangler, P.B. Sunil Kumar, and M. Laradji, Faraday Discussions, 2016, **186**, 265-275.
[53] J.D. Revalee, M. Laradji, and P.B. Sunil Kumar, J. Chem. Phys., 2008, **128**, 035102.

[54] G. S. Grest and K. Kremer, Phys. Rev. A, 1986, **33**, 3628-3631.
[55] J. Zimmerberg and S. McLaughlin, Curr. Biol., 2004, **14**, R250-R252.
[56] D. Kabaso, E. Gongadze, J. Jorgačevski, M. Kreft, U. Van Rienen, R. Zorec, and A. Iglič, Cell Mol. Biol. Lett., 2011, **16**, 398-411.
[57] W. Helfrich, Z. Naturforsch. C, 1973, **28**, 693-703.
[58] B. Różycki and R. Lipowsky, J. Chem. Phys., 2015, **142**, 054101.
[59] L. Karotki, J.T. Huiskonen, C.J. Stefan, N.E. Ziółkowska, R. Roth, M.A. Surma, N.J. Krogan, S.D. Emr, J. Heuser, K. Grünewald, and T.C. Walther, J. Cell Biol., 2011, **195**, 889-902.
[60] R. Bukasov and J.S. Shumaker-Parry, Nano Lett., 2007, **7**, 1113-1118.
[61] A. Unger, U. Rietzler, R. Berger and M. Kreiter, Nano Lett., 2009, **9**, 2311-2315.
[62] W.T. Osowiecki, X. Ye, P. Satish, K.C.Bustillo, E.L. Clark, and A.P. Alivisatos, J. Am. Chem. Soc., 2018, **140**, 8569-8577.
[63] B. Shan, Y. Zhao, Y. Li, H. Wang, R. Chen, and M. Li, Chem. Mater., 2019, **31**, 9875-9886.
[64] W. Humphrey, A. Dalke, and K. Schulten, J. Mol. Graphics, 1996, **14**, 33-38.